Fundamental mode of freely decaying laminar swirling flows

François Beaubert, Halldor Pálsson, Sylvain Lalot, Isabelle Choquet, Hadrien Bauduin

Fundamental mode of freely decaying laminar swirling flows

F. Beaubert [a], H. Pálsson [b], S. Lalot [a, *], I. Choquet [c], H. Bauduin [a]

[a] TEMPO, UVHC, Campus Mont Houy, 59313 Valenciennes Cedex 9, France
[b] University of Iceland, Sæmundargötu 2, Reykjavík 101, Iceland
[c] University West, Department of Engineering Science, Trollhättan 46186, Swede

* Corresponding author. Tel.: +33 327 511 973; fax: +33 327 511961.
E-mail addresses: francois.beaubert@univ-valenciennes.fr (F. Beaubert), halldorp@hi.is (H. Pálsson), sylvain.lalot@univ-valenciennes.fr (S. Lalot), isabelle.choquet@hv.se (I. Choquet), hadrien.bauduin@univ-valenciennes.fr (H. Bauduin)

ABSTACT

A detailed study of a swirling flow in a tube is presented in the first part of the paper. A simplified analytical solution of the governing equations indicates specific modes of the tangential velocity and that the decay of the swirl effect is exponential. The problem is then solved in three dimensions using computational fluid dynamics (CFD) and a comparison with analytical expressions shows that the CFD code is reliable in terms of accuracy.
The CFD results confirm that a fundamental swirling mode is reached within a short dis- tance from the inlet. The torque swirl number is introduced to physically estimate the intensity of the swirl. A companion value is given: it is the average deviation.

KEYWORDS

Laminar
Decay
Swirl
Analytical
Boundary condition
OpenFOAM

1. Introduction

Swirling flows are encountered in many situations, either as a consequential and sometimes unwanted effect or as an induced and controlled effect. Apart from specific utilization of swirling flow that are linked to the increased shear stresses, e.g. [1–3], they are extensively used in burners, e.g. [4–6], for their mixing ability. A specific and important purpose of swirling flow is to increase the convection heat transfer coefficient in tubes. In this context, most of the applications are related to heat exchangers, which is the topic of this paper.

There are many ways to create a swirling flow in tubes. The most widely used technique is based on twisted tapes which can either be continuous or discontinuous, see e.g. [7–9]. These tapes are easily fitted inside tubes, but their main drawback is a quite large increase in the pressure drop along the tubes. When applicability to tube bundles is not an issue, i.e. when space is available around the tube inlet, tangential inlets are often used, where the flow is rotated around the tube axis. More complex geometries are also used, as presented in e.g. [10,11]. A solution similar to the tangential inlet involves installing inserts at the entrance of the tubes, as described in e.g. [12–14]. In one such case, as detailed in [15], it has been shown that the gain in increased heat transfer because of the swirling flow might be higher than the increased pumping energy necessary to overcome the pressure loss due to the swirling flow induction. Thus, an optimal design of heat exchanger tubes can in some cases involve installation of swirling devices in a given set of specific tubes, in place of changing the tube diameters to maximize the heat flow.

DOI : 10.1016/j.apm.2016.02.002

The topic of the present paper is laminar swirling flow in a tube. It is shown in [16] that in the laminar regime the fluid equations representing the swirling flow are linear with respect to the Reynolds number, for a Reynolds number up to 1600. A Reynolds number sastifying this criterion was thus used in this study, $Re = 100$ to be specific. The aim here is to present a semi-analytical solution for the decay of the swirling flow along a tube and compare the results to ones obtained with Computational Fluid Dynamics (CFD) calculations. The overall purpose is to be able to compare with results from CFD calculations in a sufficiently accurate manner using specific inlet profiles for the swirling flow, and consequently ensure the suitability and accuracy of the CFD models in designing and testing optimal swirling flow inlet conditions. Even though most CFD models are at a mature stage with regards to accuracy, especially for laminar flow, an analytical solution with respect to well defined prerequisites is an important tool to ensure the correct physical behavior of CFD calculations and estimate discretization errors always involved in numerical methods. Such analysis results are also of great help in determining appropriate mesh densities in heat exchanger CFD modeling of the type described in the paper.

Most of the studies that have been published until now deal with turbulent flow (see e.g. [17,18]), which is by far the most common flow regime in tubes. Also, some studies have considered flow at lower Reynolds numbers and with regard to such cases a review of swirling effect for transitional flows is given in [19]. However, in the case of tube flow with highly viscous fluids the flow regime can be laminar and in such cases the number of published studies is quite limited, see e.g. [20,21].

The analytical study is presented in the first part of the paper. As a preliminary to the CFD calculations, a new boundary condition is presented in the second part of the paper, developed for the pressure at the outlet of the tube under consideration. The third part is dedicated to the validation of the computations by comparisons with selected analytical solutions. Different inlet profiles are considered and results are analyzed in the fourth part of the paper, with a special attention on the characterization of the swirling effect.

2. Analytical solution

The relations governing steady and incompressible flow are the continuity equation and the momentum equations, relating velocity and pressure, supplemented with appropriate boundary conditions. The geometry studied here is a circular tube and hence it is assumed that the velocity and pressure do not depend on the angular coordinate θ. The reduced set of equations, in cylindrical coordinates (r, θ, z), to be solved is then (the first one represents continuity)

$$\frac{1}{r}\frac{\partial r u_r}{\partial r} + \frac{\partial u_z}{\partial z} = 0 \tag{1}$$

$$\rho\left(u_r\frac{\partial u_r}{\partial r} + u_z\frac{\partial u_r}{\partial z} - \frac{u_\theta^2}{r}\right) + \frac{\partial p}{\partial r} = \mu\left(\frac{1}{r}\frac{\partial}{\partial r}\left(r\frac{\partial u_r}{\partial r}\right) + \frac{\partial^2 u_r}{\partial z^2} - \frac{u_r}{r^2}\right) \tag{2}$$

$$\rho\left(u_r\frac{\partial u_\theta}{\partial r} + u_z\frac{\partial u_\theta}{\partial z} + \frac{u_r u_\theta}{r}\right) = \mu\left(\frac{1}{r}\frac{\partial}{\partial r}\left(r\frac{\partial u_\theta}{\partial r}\right) + \frac{\partial^2 u_\theta}{\partial z^2} - \frac{u_\theta}{r^2}\right) \tag{3}$$

$$\rho\left(u_r\frac{\partial u_z}{\partial r} + u_z\frac{\partial u_z}{\partial z}\right) + \frac{\partial p}{\partial z} = \mu\left(\frac{1}{r}\frac{\partial}{\partial r}\left(r\frac{\partial u_z}{\partial r}\right) + \frac{\partial^2 u_z}{\partial z^2}\right) \tag{4}$$

where $\vec{u}(u_r, u_\theta, u_z)$ denotes the velocity, p the pressure, ρ the density, and μ the dynamic viscosity.

The system of differential equations (Eqs. 1–4) is written in a dimensionless form using $r = r^0 r^*, u_r = u_r^0 u_r^*$, $z = z^0 z^*, u_z = u_z^0 u_z^*$, $u_\theta = u_\theta^0 u_\theta^*$ and $p = p^0 p^*$ where the characteristic variables are indicated with a 0, while the dimensionless variables are indicated with a $*$ symbol. It has to be noted that r^0 and z^0 are of the same order of magnitude. According to [22], the radial velocity of a confined swirling flow is "considerably smaller than the other two components". Then it is possible to write $u_r^0 = \varepsilon_z u_z^0$ and $u_r^0 = \varepsilon_\theta u_\theta^0$ with $\varepsilon_z \ll 1$ and $\varepsilon_\theta \ll 1$. In that case, the equations are written as follows:

$$\varepsilon_z\frac{\partial r^* u_r^*}{\partial r^*} + \frac{\partial u_z^*}{\partial z^*} = 0 \tag{5}$$

$$u_z^*\frac{\partial u_z^*}{\partial z^*} + Eu^0\frac{\partial p^*}{\partial \bar{z}} + \varepsilon_z\left(u_r^*\frac{\partial u_z^*}{\partial r^*}\right) = \frac{1}{Re_r^0}\left(\frac{1}{r^*}\frac{\partial}{\partial r^*}\left(r^*\frac{\partial u_z^*}{\partial r^*}\right) + \frac{\partial^2 u_z^*}{\partial z^{*2}}\right) \tag{6}$$

$$u_z^*\frac{\partial u_\theta^*}{\partial \bar{z}} + \varepsilon_\theta\frac{u_\theta^0}{u_z^0}\left(u_r^*\frac{\partial u_\theta^*}{\partial r^*} + \frac{u_r^* u_\theta^*}{r^*}\right) = \frac{1}{Re_z^0}\left(\frac{1}{r^*}\frac{\partial}{\partial r^*}\left(r^*\frac{\partial u_\theta^*}{\partial r^*}\right) + \frac{\partial^2 u_\theta^*}{\partial z^{*2}} - \frac{u_\theta^{*2}}{r^{*2}}\right) \tag{7}$$

where Eu^0, Re_r^0 and Re_z^0 are the Euler number and Reynolds numbers.

At the 0*th* order in ε_z, the insertion of Eq. (5) in Eq. (6) leads to the classical parabolic profile for the axial velocity

$$u_z = 2u_0\left(1 - \frac{r^2}{R^2}\right) \tag{8}$$

where R denotes the pipe radius.

Now it is convenient to use the separation of variables technique to solve Eq. (3) at the 0*th* order in ε_z and ε_θ. Correspondingly, it is proposed here that the tangential velocity profile is a self-similar function, the amplitude of which decreases exponentially with the axial coordinate z

$$u_\theta(r,z) = u_{tmax}\phi(r)\exp\left(-\frac{\alpha z}{R}\right) \tag{9}$$

where u_{tmax} is the maximum tangential velocity, ϕ is the dimensionless tangential velocity profile, and α is a dimensionless scaling parameter, to be determined in the following text. Considering these assumptions, the ordinary differential equation to be solved is then

$$-\frac{\alpha\rho u_0}{R\mu}2\left(1 - \frac{r^2}{R^2}\right)\phi = \frac{1}{r}\frac{d}{dr}\left(r\frac{d\phi}{dr}\right) + \alpha^2\phi - \frac{\phi}{r^2} \tag{10}$$

Now, by introducing the dimensionless coordinate $\eta = r/R$, the dimensionless form of the equation becomes

$$\frac{1}{\eta}\frac{d}{d\eta}\left(\eta\frac{d\phi}{d\eta}\right) = \left(\frac{1}{\eta^2} - \alpha^2 - \alpha Re\left(1-\eta^2\right)\right)\phi \tag{11}$$

with

$$Re = \frac{2\rho u_0 R}{\mu} \tag{12}$$

To the authors knowledge, no analytical solutions to Eq. (11) exists and therefore an approximate solution must be obtained using a numerical procedure. Assuming no-slip condition at the pipe wall and a bounded value of the flow vorticity at the center, the necessary boundary conditions are

$$\phi(0) = \phi(1) = 0$$

Note that special care must be taken at the axis, since some of the terms in Eq. (11) go to infinity there. In order to deal with this problem the equation is solved by numerical integration, starting at the wall ($\eta = 1$) with an initial value $\phi(1) = 0$ and a guessed value for the derivative of ϕ. The equation to be solved here is an eigenvalue problem, and consequently valid solutions (i.e. leading to $\phi(0) = 0$) are obtained only for specific discrete values of the decaying parameter α. Fig. 1 shows the evolution of the value on the axis versus the value of the decaying parameter for $Re = 100$, and for a given derivative of ϕ at the wall. Note that the value of $\phi(0) = 0$ is obtained by extrapolation from the last two values (as close to the axis as possible).

The first three eigenvalues of parameter α are $\alpha_0 = 0.213179$, $\alpha_1 = 0.739503$ and $\alpha_2 = 1.563122$. The derivative is then adjusted until the maximum value of ϕ is unity in order to normalize the different eigensolutions in a consistent manner.

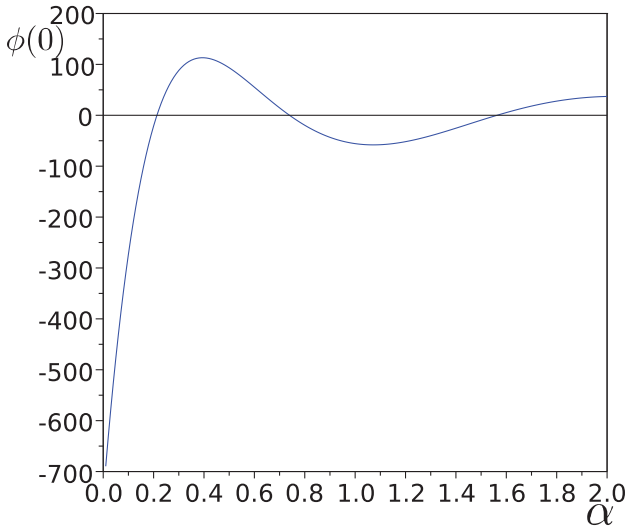

Fig. 1. Evolution of the value of ϕ on the axis versus the decaying parameter α.

DOI : 10.1016/j.apm.2016.02.002

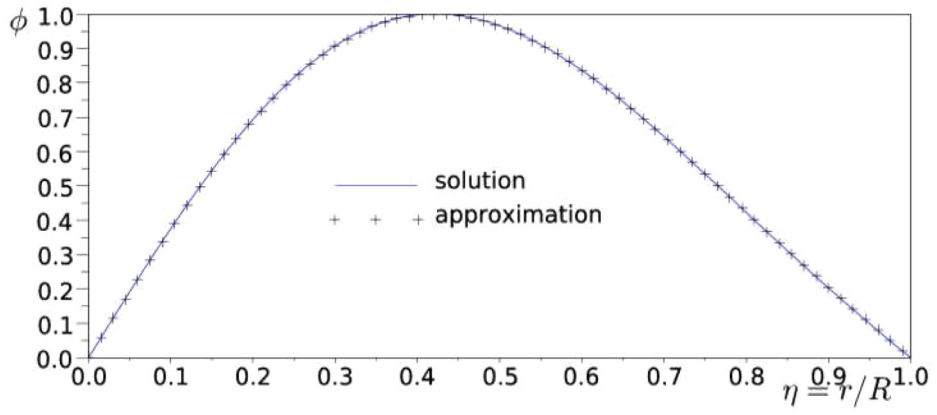

Fig. 2. Dimensionless tangential velocity profile for the first eigenvalue.

To compute an approximate value of the decaying parameter for other Reynolds numbers, it can be noted that as long as α^2 is negligible compared to αRe, the following equations are valid

$$\alpha_0 Re = 21.3179,\ \alpha_1 Re = 73.9503,\ \alpha_2 Re = 156.3122$$

Thus, the higher the Reynolds number, the lower the decaying parameter. Or, the higher the Reynolds number, the longer the effect of the swirl along the axis. This is equivalent to what is shown in Fig. 4 of [20]; the non-linear part of that particular plot will be discussed later in this paper. To strengthen this finding further, Fig. 11 of [23] clearly shows that for a Reynolds number ratio of 4, the length of the swirl effect is also in a ratio of 4.

It should be noted here that the ratios of the second and third eigenvalues to the first one indicate that the decay corresponding to these eigenvalues will be much higher than the decay corresponding to the first eigenvalue. It can be concluded that the swirling flow corresponding to the first eigenvalue is a "fundamental swirling mode". This will be confirmed later in this paper.

To easily introduce the velocity in a CFD code as an inlet boundary condition, it is convenient to write the velocity profile as a polynomial function of the dimensionless radius. Here, it was found that for the first eigensolution a sixth degree polynomial is sufficient, with a correlation coefficient of 0.9999983. Fig. 2 shows the comparison of the solution with the polynomial approximation.

The numerical results obtained for the flow considered for this study show that the radial velocity is about 100 times lower than the tangential velocity. Hence, the authors have decided not to try to find the analytical solution at the first order of ε_z and ε_θ. Nevertheless, numerical results will be presented, showing that the evolution of the radial velocity is in a very good agreement with the variation of the axial velocity profile.

It is possible to create other velocity profiles using appropriate "swirlers". To study the downstream effect of these devices, it is convenient to use a Computational Fluid Dynamics (CFD) code where the domain must be long enough to include the whole decaying process of the swirling effect. But in order to save computational time, it is clearly beneficial to shorten the domain under consideration if possible. To be able to do so, the boundary conditions should be corrected at the outlet if the swirling effect is still present, as the current available conditions do not correctly take account of a residual swirl. The next part of the paper presents a remedy for the downstream boundary conditions, using the CFD code OpenFOAM (Open Field Operation And Manipulation). OpenFOAM is an open source object-oriented numerical simulation toolkit developed in C++ and released under GPL license by the OpenFOAM® Foundation (http://www.openfoam.org). OpenFOAM is specifically tailored for both simple and advanced implementation of physical models in continuum mechanics by implementing operator-based implicit and explicit Finite Volume discretization in three dimensional space [24]. It also can be used in other domains such as electro-magnetics, stress analysis of solids, and finance.

3. CFD calculation method

In this section, the prerequisites of the numerical calculations are described, both involving the governing equations as well as specific definitions such as boundary conditions. Note that in the current study, the flow is assumed to be steady and incompressible with a strictly Newtonian fluid of constant viscosity.

3.1. Solving and meshing

The equations that are solved can be written in general form as the continuity equation

$$\nabla \cdot \vec{u} = 0 \tag{13}$$

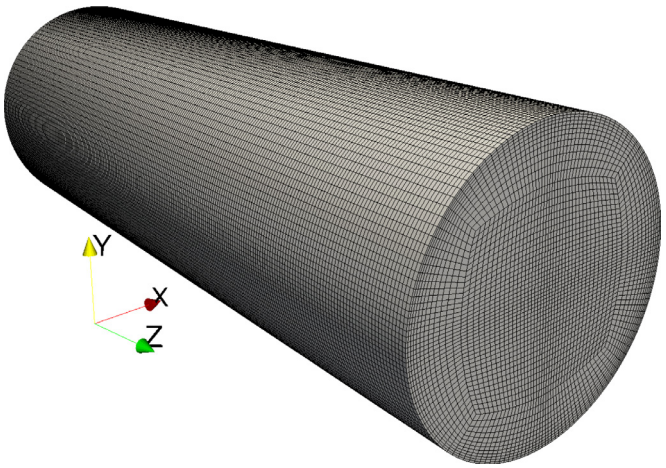

Fig. 3. Mesh used for the last computation (800 000 cells).

and the steady momentum vector equation

$$\rho\vec{u}\cdot\nabla\vec{u}+\nabla p=\mu\nabla^2\vec{u} \tag{14}$$

A standard method for solving this set of equations is to use the SIMPLE (Semi-Implicit Method of Pressure Linked Equations) algorithm, based on a pressure velocity coupling with internal iterations which account for the nonlinearity of Eq. 14, see e.g. [25]. In this iterative process, an approximation of the velocity field is obtained by solving the momentum equation where the pressure gradient term is calculated using the pressure distribution from the previous iteration. The pressure equation is then formulated and solved in order to obtain a new pressure distribution. Velocities are then corrected using the pressure correction to ensure the incompressibility constraint implied by the continuity equation. More details can be found in [26]. This is the method applied in the numerical code used in the computations, referred to as the OpenFOAM solver `simpleFoam`. The convergence criteria of the iterative solvers are based on the residuals values of the different flow field variables. Convergence criteria were set to a value of 10^{-10} for the pressure and 10^{-16} for the velocity field.

Flexibility in mesh handling is provided by supporting block structured hexahedral meshes as well as unstructured polyhedral meshes with topological changes. Efficiency of execution is achieved by the use of iterative methods for linear systems, notably Preconditioned Conjugate Gradient and Algebraic Multigrid solvers, and the use of massively parallel computers and domain decomposition. In the present study, a block structured mesh is created using the `blockMesh` application (OpenFOAM mesher) and is composed of hexahedra elements in order to minimize numerical diffusion and maximize computational efficiency (Fig. 3).

3.2. Boundary conditions

The boundary conditions for the inlet are presented as a predefined velocity profile with an axial term u_z along the tube and a tangential term u_θ representing the swirling flow. The pressure is defined as having a zero gradient perpendicular to the inlet surface, equivalent to $\partial p/\partial n=0$. Note that it makes possible a variation of the pressure in the radial direction. At the wall, the no-slip condition is applied, i.e. $u_r=u_\theta=u_z=0$, and the normal gradient of the pressure is set to zero, just as for the inlet.

For the outlet, the velocity components are assumed to have a zero normal gradient, which is the usual procedure for a free outlet in internal flows. However, a new boundary condition has been developed for the pressure since the usual assumption of a fixed pressure over the whole outlet surface does not hold for a rotating flow. Thus, the pressure must be defined in a consistent manner, taking into account the upstream pressure condition as well as the centrifugal effect, seen in Eq. 2. Therefore, it has been decided to define a new boundary condition which is based on the extrapolation of the pressure in the boundary cell and its closest internal neighbor (Fig. 4). In fact, the pressure gradient is assumed to be locally constant. As a result, the boundary face pressure p_{bf} is set according to $p_{bf}=p_{bc}+(p_{bc}-p_{ic})\frac{(\vec{x}_{bf}-\vec{x}_{bc})\cdot\vec{n}_{bf}}{(\vec{x}_{bc}-\vec{x}_{ic})\cdot\vec{n}_{if}}$ where p is the pressure, $\vec{x}$ the location, $\vec{n}$ the unit vector normal to a face, and the indexes *bf, if, bc*, and *ic* denote the boundary face center, the first inner face center, the boundary cell center, and the first inner cell center respectively (see Fig. 4). This boundary condition has been implemented in the CFD software OpenFOAM. Since the latter is developed for non-structured meshes, the information needed at the different cell and face centers is accessed based on the boundary faces as shown by the algorithmic procedure in Fig. 5). A special care has been taken in ensuring that the computational domain could be on the left hand side or the right hand side of the boundary face. Further details are found in the accompanying

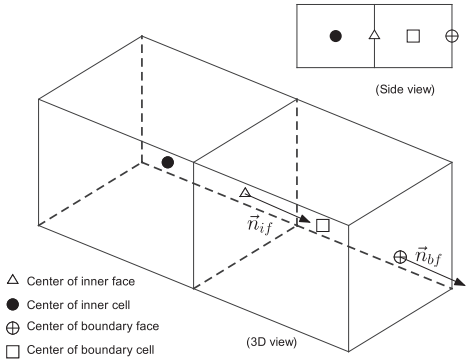

Fig. 4. Schematic of the cells close to the boundary.

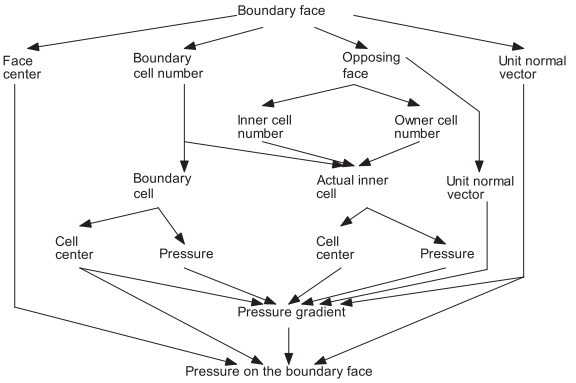

Fig. 5. Algorithmic procedure to determine the pressure on the boundary face.

files (extrapolPressureOrder1FvPatchScalarField.C and extrapolPressureOrder1FvPatchScalarField.H) on the Elsevier website. Note that for numerical reasons, it is not possible to set the same boundary condition at the inlet when it is already set at the outlet.

OpenFOAM being fundamentally a 3D solver, the implementation of the procedure is done only for 3D meshes. This has been intentionally done as the authors intend to study later turbulent flows for which 3D effects occur. Furthermore, it has been shown that 2D axisymmetric computations do not lead to good results when dealing with swirling flows for which three-dimensional effect can be expected (e.g. [27,28]).

3.3. Validation

The new boundary condition had to be validated by some means. As a first step, this was done by using a well known problem: the entrance zone of a laminar flow in a circular tube. The inlet velocity is constant over the entire inlet surface. It is known that the entrance length L_e, i.e. the distance needed by the fluid to get the standard parabolic velocity profile, is linked to the Reynolds number according to the following approximation:

$$L_e/D = 0.06Re \tag{15}$$

The Reynolds number has been chosen as 100 in this study, so that the entrance length is $L_e = 6D$. An initial computation was based on a computational domain which has a length of $20D$; much longer than the entrance length. In this case the gage pressure is set to zero on the entire outlet surface. After a standard mesh dependency study based on the convergence of the velocity profiles at various axial locations, the results obtained were used as reference. Then a $6D$ long domain was considered (which is the sufficient entrance length according to Eq. 15) and the results obtained using the new boundary condition were compared to the reference results. Note that the size of the cells are the same for both meshes so that no space discretization effect is induced (the number of discretization points on the z axis for the 20D long domain is three times the number of discretization points on the z axis for the 6D long domain).

Figs. 6 and 7 show that the velocity is well predicted (the axial velocity on the axis and at $r = R/2$ as well as the radial distribution of the axial velocity at $z = 2D$, $z = 4D$, and $z = 6D$).

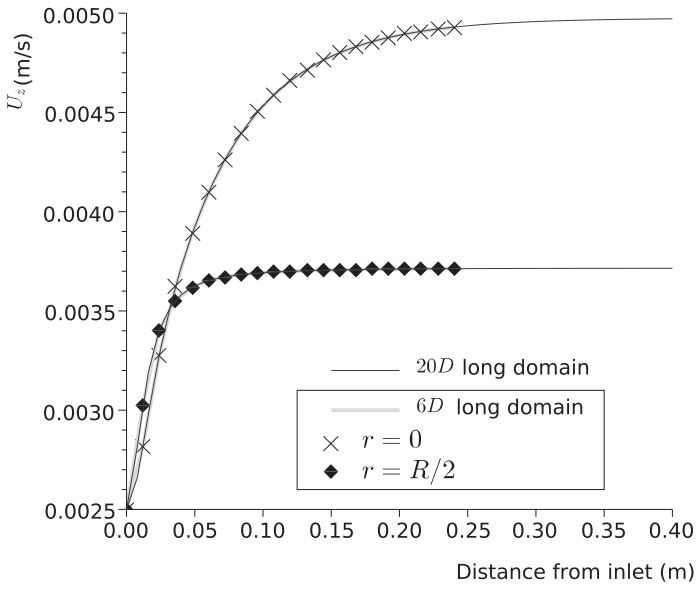

Fig. 6. Axial velocity u_z at two radial locations.

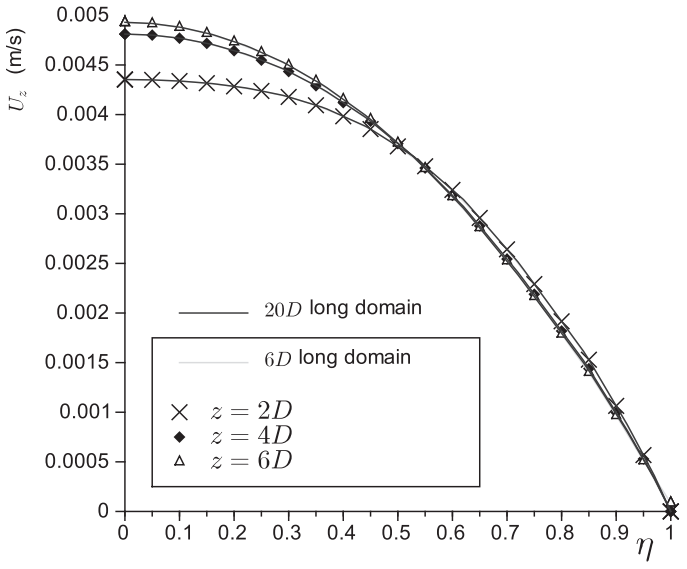

Fig. 7. Radial distribution of the axial velocity profile at three axial locations.

The second validation test was carried out for a swirling flow using Eq. 8 for the axial velocity and the polynomial approximation for the tangential velocity. For this case the maximum tangential velocity is $U_{tmax} = 0.002\, m/s$. Fig. 8 shows the comparison of the computed results with the analytical expression (Eq. 9) at $r = R/4$.

At the inlet of the computational domain the zero-gradient boundary condition is applied. At the outlet of the computational domain, either the standard constant pressure condition or the newly developed condition are applied. Fig. 9 shows the difference between what is obtained using these two conditions. It can be observed that the influence of the outlet boundary condition is still visible at about $1/2\,D$ inside the computational domain. It can be concluded that it is necessary to use the new boundary condition.

Fig. 10 shows the comparison of the computed dimensionless tangential velocity with the approximation given by the sixth degree polynomial. The very good agreement shows that the assumptions made to obtain the polynomial are correct.

Fig. 11 shows the evolution of the tangential velocity U_θ for three radial locations ($R/4$, $R/2$, $3R/4$).

DOI : 10.1016/j.apm.2016.02.002

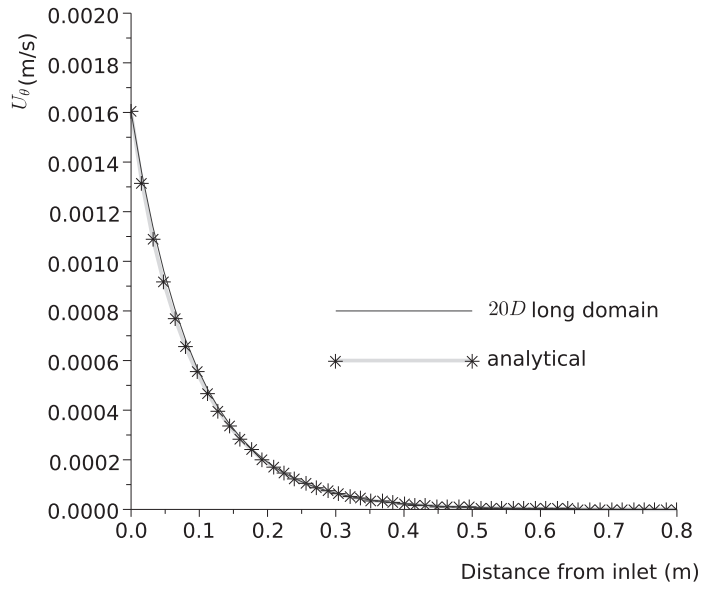

Fig. 8. Comparison of the computed tangential velocity with the analytical expression at $r = R/4$.

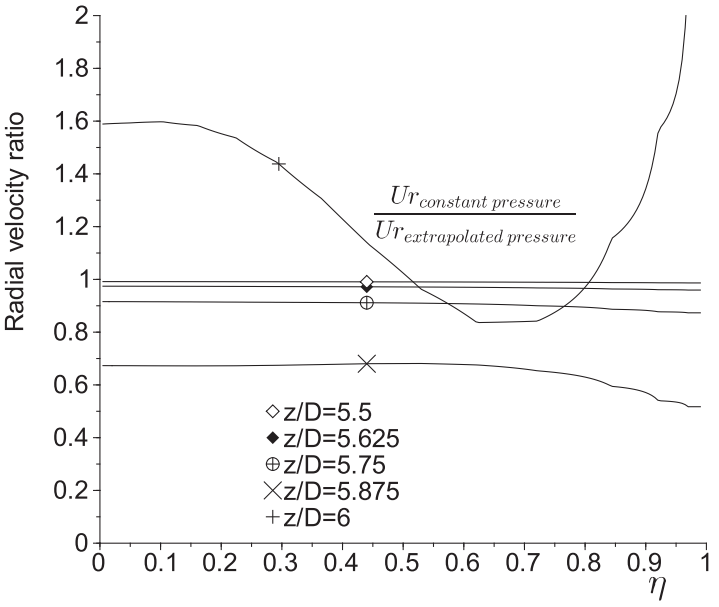

Fig. 9. Comparison of the radial velocity profile obtained using the standard outlet condition with the profile obtained using the new boundary condition at the outlet of the 6D computational domain.

Fig. 12 shows the comparison of the tangential velocity profiles at four axial locations (inlet, $z = 2D$, $z = 4D$, and $z = 6D$). Fig. 13 shows the evolution of the pressure on three axial lines.

All-together, Figs. 7–13 show that the computed solution is very close to the analytical solution and that the new boundary condition is efficient and provides very accurate results.

It is now possible to examine results concerning the radial velocity. Fig. 14 shows the evolution of the radial velocity, depending on the axial location. The curves are obtained by approximating each computed result by a sixth degree polynomial in order to be able to estimate the derivative with respect to the radius. Fig. 15 shows that the decay of the radial velocity is similar to the decay of the tangential velocity. From this curve it is possible to estimate the maximum radial velocity at the inlet: $23.18 \times 10^{-6} m/s$ which is about 100 times lower that the maximum tangential velocity.

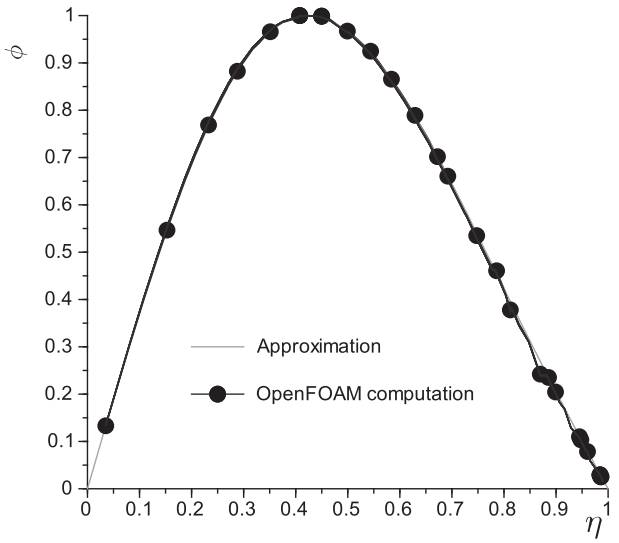

Fig. 10. Comparison of the computed radial distribution of the dimensionless tangential velocity with the approximation given by the sixth degree polynomial.

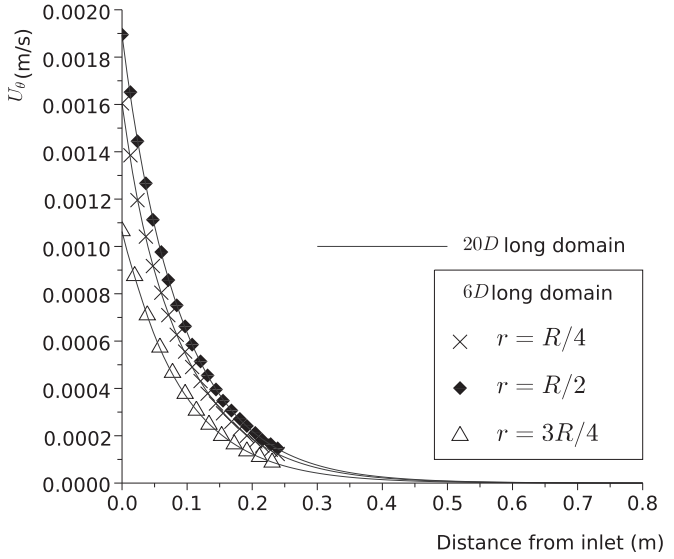

Fig. 11. Axial distribution of the tangential velocity for two different lengths of the computational domain at three radial locations.

Fig. 16 shows the evolution of the derivative of the axial velocity with respect to the axial location. The latter is obtained from Eq. 1. It can be noted that the results are in very good agreement with the results shown in Fig. 17. In particular, the location of the point having no variation is well predicted.

4. Application to alternative swirling flows

Since Eq. 11 is linear, it is possible to build a solution as a linear combination of the solutions obtained for e.g. the first three eigenvalues (Fig. 18).

But to characterize these profiles in a simple and descriptive way, a swirl number should be defined. Various swirl numbers have been defined for swirling flows and among them, two are mentioned here: the geometric swirl number

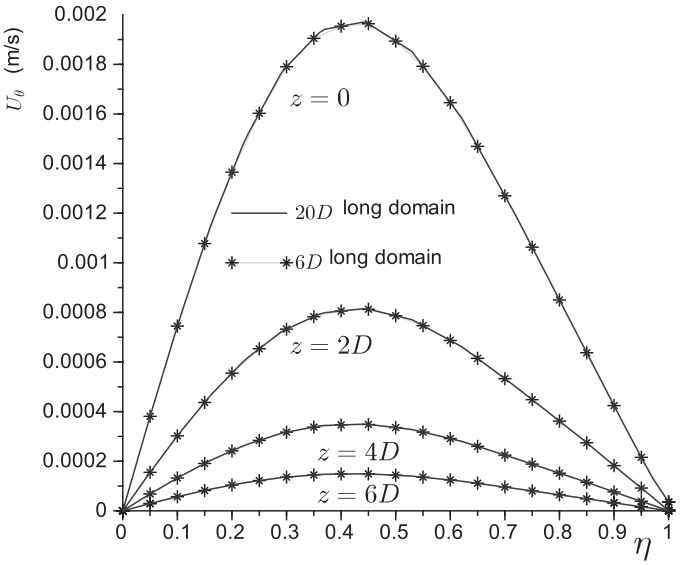

Fig. 12. Tangential velocity profiles for two different lengths of the computational domain at four axial locations.

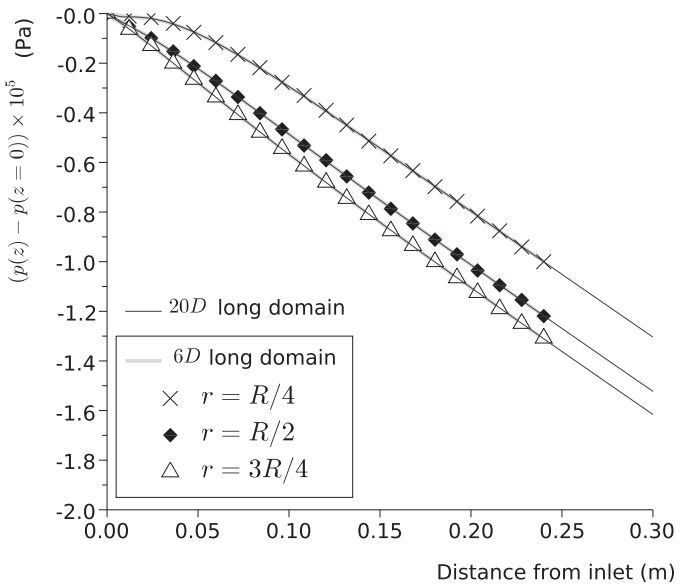

Fig. 13. Pressure profiles for two different lengths of the computational domain at three radial locations.

defined as $S_G = \frac{\overline{U_\theta}}{\overline{U_z}}$ (see e.g. [29]) and what is usually called the swirl number, first defined in [30] as

$$S = \frac{\rho r u_\theta u_z dA}{R \quad \rho u_z u_z dA} \tag{16}$$

Although the numerator of this expression has a physical meaning as reminded hereafter, the denominator is an arbitrary expression (torque due to axial forces computed using the radius of the tube). The authors of this paper believe that a new swirl number having a better physical significance can be defined. The fluid flowing out from a tube section containing a swirler would provide a torque expressed as follows:

$$T_s = \quad r u_\theta d\dot{m} \tag{17}$$

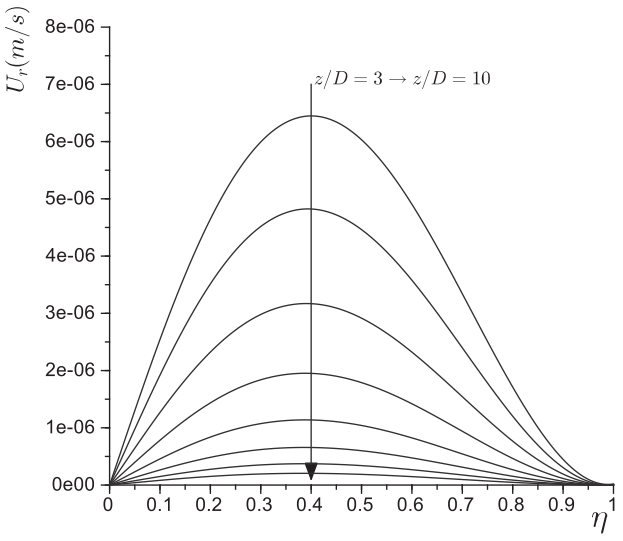

Fig. 14. Evolution of the radial velocity profile from $z/D = 3$ to $z/D = 10$.

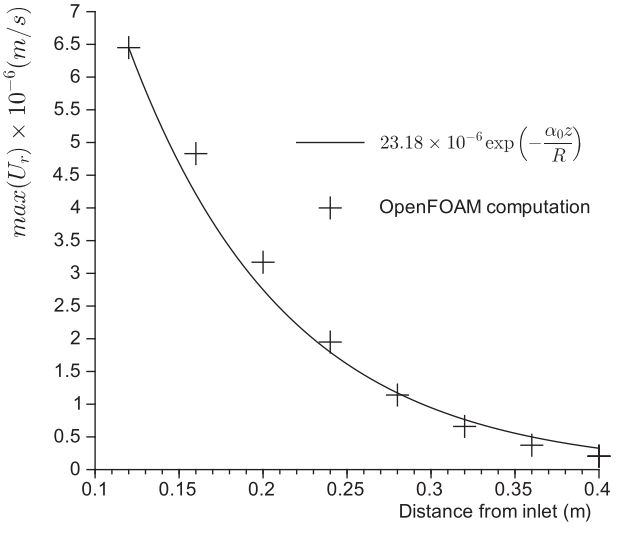

Fig. 15. Evolution of the maximum radial velocity from $z/D = 3$ to $z/D = 10$.

which is equivalent to the numerator in Eq. 16. This can be expressed as (knowing that $u_\theta = \phi u_{tmax}$):

$$T_s = 2\pi u_{tmax} R^3 \quad \eta^2 \phi u_z \rho d\eta \tag{18}$$

using η as defined in Section 2.

Considering a solid body rotation, the tangential velocity would be $u_\theta = \omega r$ and when inserted into Eq. 17, the torque would then be expressed by

$$T_b = 2\pi \omega R^4 \quad \eta^3 \rho u_z d\eta \tag{19}$$

Considering the same maximum tangential velocity, the angular velocity would be $\omega_{ref} = u_{tmax}/R$ and Eq. 18 would then become

$$T_{ref} = 2\pi \omega_{ref} R^4 \quad \eta^2 \phi u_z \rho d\eta \tag{20}$$

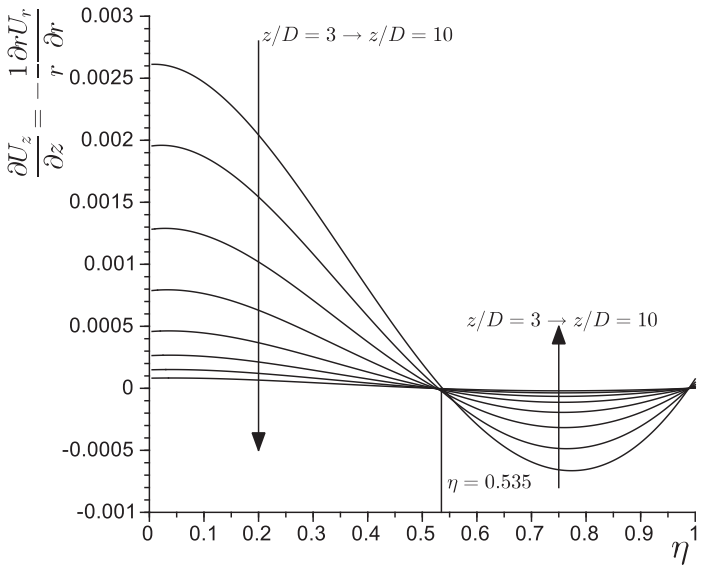

Fig. 16. Evolution of $\partial u_z/\partial z$ from $z/D = 3$ to $z/D = 10$.

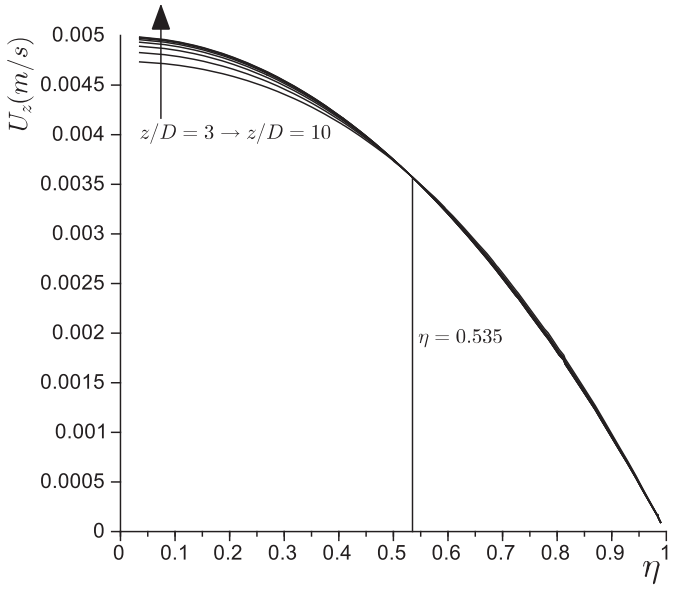

Fig. 17. Evolution of the axial velocity profile from $z/D = 3$ to $z/D = 10$.

Assuming that the solid body rotation torque equals the reference torque, a new swirl number can be presented, namely the torque swirl number

$$S_T = \frac{\omega}{\omega_{ref}} = \frac{\eta^2 \phi u_z \rho d\eta}{\eta^3 u_z \rho d\eta} \tag{21}$$

It can be noticed that in a first approximation ($0th$ order in ε_z and ε_θ) this swirl number depends only on the dimensionless tangential velocity profile, and thus does not depend on the axial location once the standard tangential velocity profile is obtained. Note that in that case it is also possible to compute the maximum value of the torque swirl number which would correspond to a constant dimensionless tangential velocity profile ($\phi = 1$): $(S_T)_{max} = \frac{\int \eta^2 u_z \rho d\eta}{\int \eta^3 u_z \rho d\eta} = \frac{24}{15} = 1.6$. The minimum value of S_T is 0 for a non-swirling flow, and its mean value is 0.8. Eq. 21 clearly shows that if $\phi = \eta$ the torque swirl number is unity which is equivalent to a solid body rotation. It also shows that if the maximum value of the tangential velocity is close to the axis of the tube, the torque swirl number can be less than unity; and that if this maximum is close

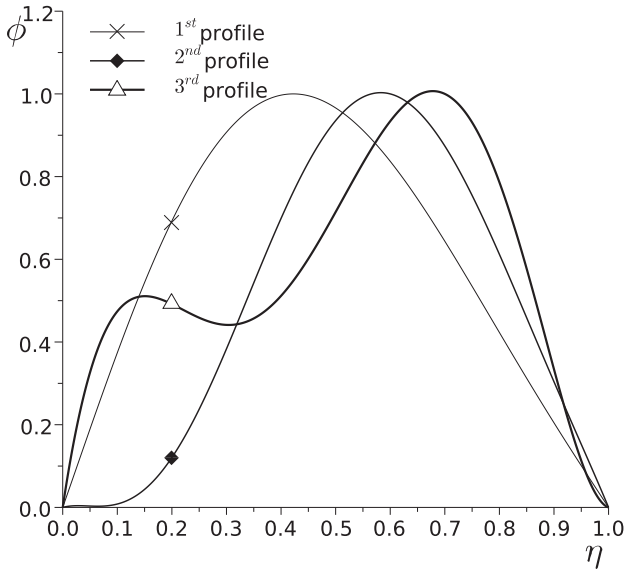

Fig. 18. The three dimensionless tangential velocity profiles.

to the tube wall the torque swirl number is greater than unity. The latter point is confirmed hereafter. It can be concluded that this new swirl number can give information on the shape of the tangential velocity profile compared to the solid body rotation velocity profile along with the intensity of the swirl. This is an advantage compared to the standard swirl number.

The torque swirl number of the three studied tangential velocity profiles are $S_T = 1.083$, $S_T = 1.130$, and $S_T = 1.151$ for the first, second and third profiles respectively. This indicates that the swirling flows considered in this study have torque swirl numbers higher than the mean torque swirl number $\left(\overline{S_T} = 0.8\right)$.

In fact, these swirl numbers characterize the intensity of the rotation, but not the deviation from the axis and therefore a companion measure must be added to the study. Now let $\theta = \arctan\left(u_\theta/u_z\right)$ denotes the deviation of the flow from the axis. The companion measure is presented as the mean deviation and is then measured as follows:

$$\overline{\theta} = \frac{1}{A} \quad \theta dA \tag{22}$$

It should be noted that the evolution of this average deviation will be similar to the evolution of the tangential velocity: an exponential decrease as mentioned in [16] and [31], and in e.g. [21] and [32] for the standard swirl number.

Fig. 19 shows the deviation angle for the three studied profiles at the inlet.

It is found that the average deviations at the inlet are $\overline{\theta} = 24.38^\circ$, $\overline{\theta} = 28.03^\circ$, and $\overline{\theta} = 27.80^\circ$ for the first, second and third tangential velocity profiles respectively. Note that the deviation angle of the third velocity profile (having the highest torque swirl number) is lower than the deviation angle of the second velocity profile. This confirms that both information are necessary to characterize the swirl.

Fig. 20 shows the comparison of the computed tangential velocity at $\eta = 0.5$ for the second profile with the following analytical equation:

$$\lambda_0 \exp\left(-\alpha_0 z/R\right) + \lambda_1 \exp\left(-\alpha_1 z/R\right) = 0.0016 \exp\left(-0.213179 z/R\right) + 0.0002 \exp\left(-0.739503 z/R\right)$$

It can be noted that the effect of the second term is negligible (0.2%) compared to the first term at about $z = 4D$.

Fig. 21 shows the comparison of the computed tangential velocity at $\eta = 0.75$ for the third profile with the following analytical equation:

$$\begin{aligned}&\lambda_0 \exp\left(-\alpha_0 z/R\right) + \lambda_1 \exp\left(-\alpha_1 z/R\right) + \lambda_2 \exp\left(-\alpha_2 z/R\right)\\ &\quad = 0.0009 \exp\left(-0.213179 z/R\right) + 0.0004 \exp\left(-0.739503 z/R\right) + 0.0004 \exp\left(-1.563122 z/R\right)\end{aligned}$$

Figs. 20 and 21 show a very good agreement between the computed results and the analytical expressions. It must be noted that the effect of the third term is negligible (0.2%) compared to the first term at about $z = 1.5D$; and that the second term is also negligible (0.2%) at about $z = 4D$.

As already mentioned, Fig. 4 of [19] shows a non-linear part close to the inlet. This can be explained by what has just been shown in the relations and corresponding figures above. The fluid, whatever the inlet profile, tends to turn to its "fundamental swirling mode" when developing downstream along the pipe. This is illustrated in Fig. 22. For this particular swirling mode, the torque swirl number is the one obtained for the first velocity profile: $S_T = 1.083$.

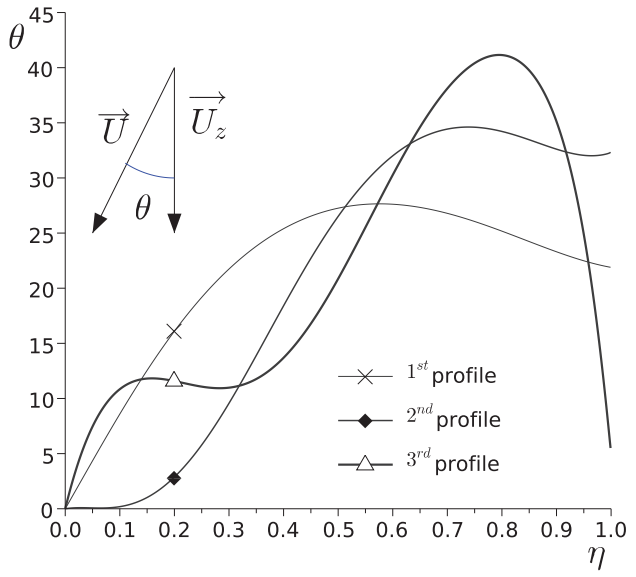

Fig. 19. Deviation angle at the inlet for the three studied profiles.

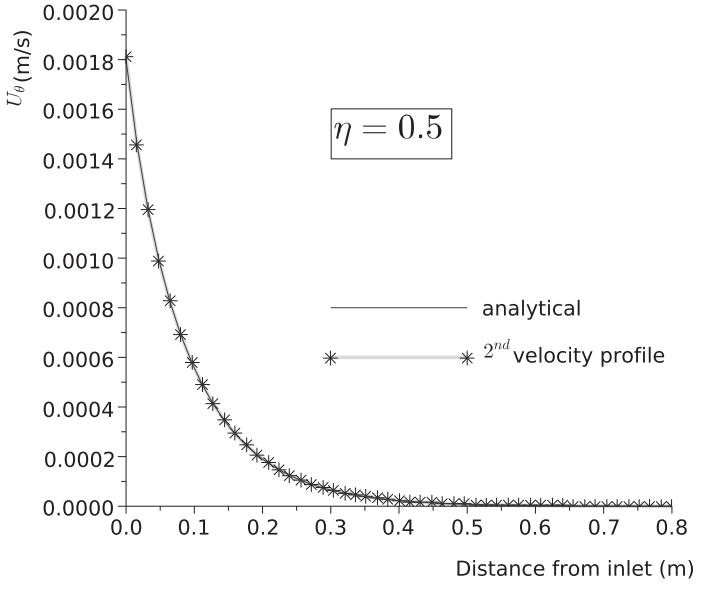

Fig. 20. Tangential velocity decay for the second profile at $\eta = 0.5$.

5. Conclusion

It has been shown that there is a fundamental swirling mode corresponding to a fundamental tangential velocity profile. Although an entrance effect takes place close to the inlet of the tube (up to $z = 4D$ for the two cases studied here), the tangential velocity profile is quickly reduced to this fundamental tangential velocity profile. It has been shown that the length of this entrance effect depends on the Reynolds number. It is believed that it also depends on the swirl intensity and on the average deviation. The findings here support that claim in a clear manner.

It has been shown that the decay of the swirl is exponential. This decay is now explicitly linked to the Reynolds number, which has clearly been demonstrated with CFD calculations and analytical derivations. This is in very good agreement with what is presented in [16]. Using the values given in that paper, the first eigenvalue would have been $\alpha_0 = 0.205$ ($\alpha_0 = 0.213179$ in the present study). It has been observed that the radial velocity also decays exponentially with the same expontial coefficient.

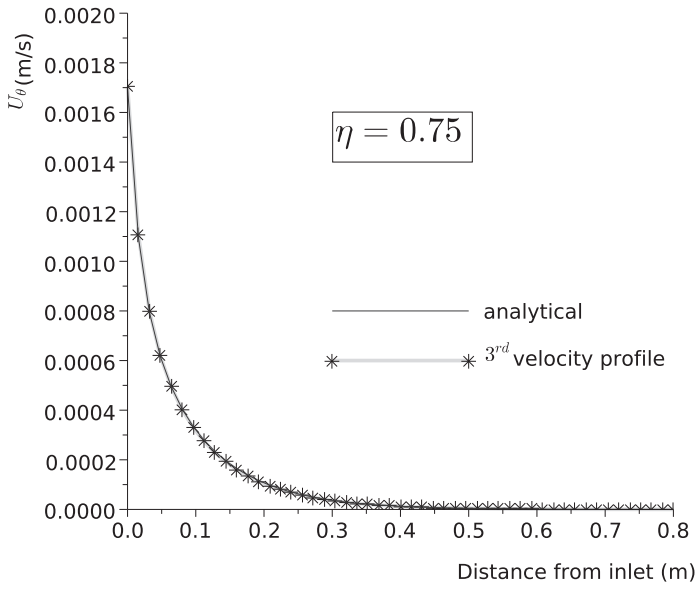

Fig. 21. Tangential velocity decay for the third profile at $\eta = 0.75$.

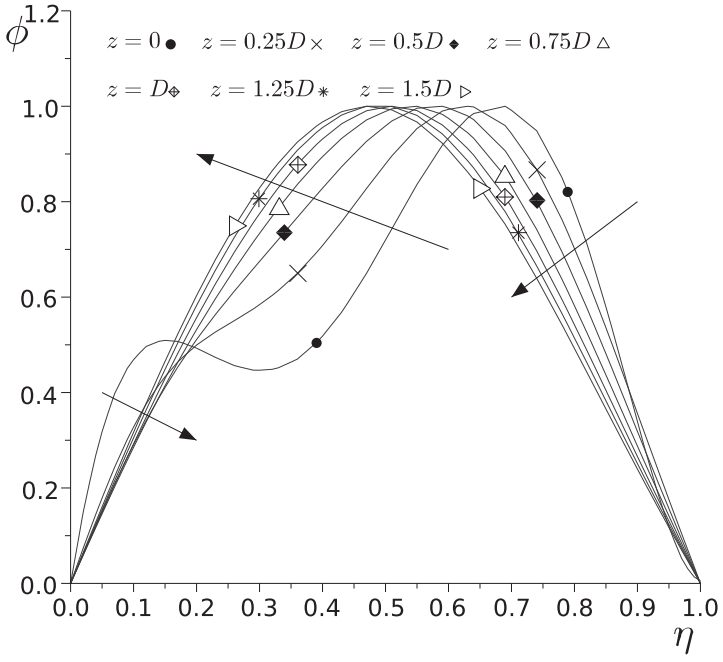

Fig. 22. Evolution of the third dimensionless tangential velocity profile versus the axial location. The arrows illustrate the curve evolutions when moving downstream.

A new swirl number has been introduced, referred to as the torque swirl number, having a more physical meaning than the one usually used in swirling flow studies. It has been shown that the fundamental tangential velocity profile corresponds to a torque swirl number of 1.083; the maximum value of this torque swirl number being 1.6.

It has also been convenient to define a new boundary condition for the pressure at the outlet of the computational domain to be able to shorten this computational domain and thus the computational cost.

Further studies will address the effect of the swirl on pressure drop and on the wall shear stress, so that it will be possible to determine if a given inlet profile has an overall benefit (heat transfer higher than pressure drop). After this analysis, the design of the swirler device will be addressed following the procedure presented in [16].

DOI : 10.1016/j.apm.2016.02.002

Acknowledgments

The authors are grateful to the Université de Valenciennes et du Hainaut-Cambrésis for the financial support of the "FISF" project (Fundamentals of Internal Swirling Flows). The Ph.D student, who is one of the authors, is supported by the French Government. This financial support is also greatly acknowledged.

The authors would like to thank Pr. Desmet and Pr. Monnoyer at the Université de Valenciennes et du Hainaut-Cambrésis for the very fruitful discussions on the physics of swirling flows, that has lead to the new definition of the swirl number, and for the very useful advices on the use of the CFD code.

The authors also would like to thank the reviewers for their very constructive comments.

Supplementary materials

Supplementary material associated with this article can be found, in the online version, at doi:10.1016/j.apm.2016.02.002.

References

[1] F. Zhan, Y. Fan, X. Deng, Swirling flow created in a glass tube suppressed platelet adhesion to the surface of the tube: Its implication in the design of small-caliber arterial grafts, Thromb. Res. 125 (2010) 413–418.
[2] A.S. Shehata, S.A. Nosier, G.H. Sedahmed, The role of mass transfer in the flow-induced corrosion of equipments employing decaying swirl flow, Chem. Eng. Process. 41 (2002) 659–666.
[3] P. Legentilhomme, P. Jaouen, Improvement of the performance of the ultrafiltration of bentonite suspensions using a swirling decaying annular flow: comparison with tangential plane and axial annular flows, o. morineau-thomas, J. Membr. Sci. 193 (2001) 19–33.
[4] T. O'Doherty, P. Bowen, The effect of hydrogen containing fuel blends upon flashback in swirl burners, nicholas syred, mohammed abdulsada, anthony griffiths, Appl. Energy 89 (2012) 106–110.
[5] P. Heil, D. Toporov, H. Stadler, S. Tschunko, M. Förster, R. Kneer, Development of an oxycoal swirl burner operating at low o2 concentrations, Fuel 88 (2009) 1269–1274.
[6] L. Zeng, Z. Li, G. Zhao, J. Li, F. Zhang, S. Shen, L. Chen, The influence of swirl burner structure on the gas/particle flow characteristics, Energy 36 (2011) 6184–6194.
[7] S.K. Saha, A. Dutta, S.K. Dhal, Friction and heat transfer characteristics of laminar swirl flow through a circular tube fitted with regularly spaces twisted-tape elements, Int. J. Heat Mass Transf. 44 (2001) 4211–4223.
[8] K. Wongcharee, S. Eiamsa-ard, Friction and heat transfer characteristics of laminar swirl flow through the round tubes inserted with alternate clockwise and counter-clockwise twisted-tapes, Int. Commun. Heat Mass Transf. 38 (3) (2011) 348–352.
[9] R. Cazan, C.K. Aidun, Experimental investigation of the swirling flow and the helical vortices induced by a twisted tape inside a circular pipe, Phys. Fluids 21 (2009) 037102.
[10] F. Chang, V.K. Dhir, Mechanisms of heat transfer enhancement and slow decay of swirl in tubes using tangential injection, Int. J. Heat Fluid Flow 16 (1995) 78–87.
[11] J. Wang, G.H. Priestman, J.R. Tippetts, Modelling of strongly swirling flows in a complex geometry using unstructured meshes, Int. J. Numer. Meth. Heat Fluid Flow 16 (8) (1991) 910–926.
[12] A.F. Najafin, S.M. Mousavian, K. Amini, Numerical investigations on swirl intensity decay rate for turbulent swirling flow in a fixed pipe, Int. J. Mech. Sci. 53 (2011) 801–811.
[13] I. Kurtbaş, F. Gülçimen, A. Akbulut, D. Buran, Heat transfer augmentation by swirl generators inserted into a tube with constant heat flux, Int. Commun. Heat Mass Transf. 36 (2009) 865–871.
[14] M. Yilmaz, O. Comakli, S. Yapici, O.N. Sara, Heat transfer and friction characteristics in decaying swirl flow generated by different radial guide vane swirl generators, Energy Convers. Manag. 44 (2003) 283–300.
[15] S. Eiamsa-ard, S. Rattanawong, P. Promvonge, Turbulent convection in round tube equipped with propeller type swirl generators, Int. Commun. Heat Mass Transf. 36 (2009) 357–364.
[16] F. Beaubert, H. Pálsson, S. Lalot, I. Choquet, H. Bauduin, Design of a device to induce swirling flow in pipes - a rational approach, Comptes rendus mécanique de l'Académie des Sciences 343 (1) (2015) 1–12.
[17] A. Escue, J. Cui, Comparison of turbulence models in simulating swirling pipe flows, Appl. Math. Model. 34 (10) (2010) 2840–2849.
[18] K.M. Saqr, et al., Computational study of decaying annular vortex flow using the $re_\varepsilon/\kappa - \varepsilon$ turbulence model, Appl. Math. Modell. (2011), doi:10.1016/j.apm.2011.11.082.
[19] A.F. Ryzhkov, L. Zhargalkhuu, N.S.M. Sharif, A.D. Makhaev, Estimation of the thermohydraulic efficiency of swirlers at small reynolds numbers, J. Eng. Phys. Thermophys. 82 (1) (2009) 21–28.
[20] A.M. Jawarneh, G.H. Vatistas, A. Ababneh, Analytical approximate solution for decaying laminar swirling flows within a narrow annulus, Jordan J. Mech. Ind. Eng. 2 (2) (2008) 101–109.
[21] T.F. Ayinde, Sādhanā, A generalized relationship for swirl decay in laminar pipe flow, Acad. Proc. Eng. Sci.- Indian Acad. Sci. 35 (Part 2) (2010) 129–137.
[22] X. Lu, S. Wang, H.-G. Sung, S.-Y. Hsieh, V. Yang, Large-eddy simulations of turbulent swirling flows injected into a dump chamber, J. Fluid Mech. 527 (2005) 171–195.
[23] H. Pálsson, F. Beaubert, S. Lalot, Increased shear stress in annular swirling flow for reduced fouling rate, in: Proceedings of the International Conference "Heat Exchanger Fouling and Cleaning", Fodele, Greece, June 05-10, 2011.
[24] H.G. Weller, G. Tabor, H. Jasak, C. Fureby, A tensorial approach to computational continuum mechanics using object orientated techniques, Comput. Phys. 12 (6) (1998) 620–631.
[25] S.V. Patankar, Numerical heat transfer and fluid flow, in: Series in computational methods in mechanics and thermal sciences, Taylor & Francis, 1980. ISBN: 0-89116-522-3.
[26] H.K. Versteeg, W. Malalasekera, An Introduction to Computational Fluid Dynamics: The Finite Volume Method, 2nd edition, Pearson Prentice Hall, 2007. ISBN13: 9780131274983.
[27] R.F. Susan-Resiga, S. Muntean, C. Tănasă, A. Bosioc, Three-dimensional versus two-dimensional axisymmetric analysis for decelerated swirling flows, in: Proceedings of the 14th Conference on Fluid Flow Technologies, Budapest, Hungary, September 9-12, 2009.
[28] A.S. Ćoćić, M.R. Lečič, S.M. Čantrak, Numerical analysis of axisymmetric turbulent swirling flow in circular pipe, Therm. Sci. 18 (2) (2014) 493–505.
[29] J. Kuneš, Dimensionless Physical Quantities in Science and Engineering, Elsevier, 2012. ISBN: 978-0-12-416013-2.
[30] N.A. Chigier, J.M. Beer, Velocity and static pressure distributions in swirling air jets issuing from annular and divergent nozzles, J. Basic Eng., Trans. ASME Ser. D 86 (1964) 788–796.
[31] H.Y. Hsieh, A. Spetz, J.N. Zemel, Pyroelectric anemometry: vector and swirl measurements, Sens. Actuators A: Phys. 49 (3) (1995) 141–147.
[32] M. Kiya, S. Fukusako, M. Arie, Laminar swirling flow in the entrance region of a circular pipe, Bull. JSME 14 (73) (1971-07) 659–670.